PAPER

Peierls–Nabarro stresses of dislocations in monoclinic cyclotetramethylene tetranitramine (β-HMX)

IOP Publishing Modelling and Simulation in Materials Science and Engineering
Modelling Simul. Mater. Sci. Eng. **26** (2018) 045005 (21pp) https://doi.org/10.1088/1361-651X/aab45a

Peierls–Nabarro stresses of dislocations in monoclinic cyclotetramethylene tetranitramine (β-HMX)

Anirban Pal and Catalin R Picu[1]

Department of Mechanical, Aerospace and Nuclear Engineering, Rensselaer Polytechnic Institute, Troy, NY 12180, United States of America

E-mail: picuc@rpi.edu

Received 3 January 2018, revised 1 March 2018
Accepted for publication 6 March 2018
Published 4 April 2018

Abstract

HMX (cyclotetramethylene tetranitramine) is an energetic material which releases substantial amounts of energy upon decomposition. The role of defects and deformation in causing reaction initiation was discussed in the literature but remains insufficiently understood. In this work, we identify, using computational methods, the slip systems which are potentially active in β-HMX and rank them in terms of their propensity for slip. To this end, we develop first a tentative ranking based on the degree of steric hindrance associated with slip. This is quantified using a geometric analog of the γ-surface. Further, we use atomistic models to compute the Peierls–Nabarro (PN) stress for the motion of dislocations in the slip systems with smallest degree of steric hindrance. A complex mechanical behavior is observed, including strong slip asymmetry, twinning and cleavage. The five systems with the lowest PN stress are $(011)[01\bar{1}]$, $(011)[100]$, $(101)[010]$, $(101)[10\bar{1}]$ and $(021)[100]$. We conclude that the material has enough slip systems available for supporting a generalized state of plastic strain provided the twinning system $(101)[10\bar{1}]$ is taken into consideration and that the resolved shear stress is at least 260 MPa.

Supplementary material for this article is available online

Keywords: Peierls stress, HMX, monoclinic crystal

(Some figures may appear in colour only in the online journal)

[1] Author to whom any correspondence should be addressed.

1. Introduction

Plasticity in crystalline energetic materials has garnered attention owing to its proposed role in thermo-mechanical energy localization or 'hot spot' formation during initiation [1–3]. The ability of the crystal to dissipate strain energy associated with mechanical impact depends on the formation and evolution of microstructural crystal defects such as dislocations, twins and cracks. It has been shown that impact sensitivity depends on crystal orientation, the material being more sensitive in orientations in which the shock produces limited plastic deformation [4–6]. Thus, an accurate understanding of the properties of dislocations and twins in such materials becomes important for controlling initiation and explosive safety.

Cyclotetramethylene tetranitramine (HMX) is an important secondary energetic material used in a variety of plastic bonded explosives [7, 8]. The HMX molecule is centrosymmetric and comprises an eight-membered chair-like ring of alternating carbon and nitrogen atoms, with each nitrogen atom attached to a nitro group [9]. Among the various solid phases of the crystal (α, β, γ, δ, ε) [10–12], the monoclinic β phase is stable in ambient conditions and has the highest density [13].

Characterizing plasticity caused by mechanical deformation in β-HMX has been a subject of several investigations. Palmer and Field [14] conducted compression, indentation, and etching studies on HMX and reported the formation of (101) twins and {011} cracks. The {011} family comprises the symmetrically equivalent (011) and (01$\bar{1}$) planes. Cady [15] also communicated that strained HMX crystals form (101) twins which are reversible upon load removal when created under small strains, and irreversible under large strains and at temperatures above 373 K. The twin direction and mechanism were subsequently proposed by Armstrong *et al* [16] who indicated that the twin system is (101)[10$\bar{1}$]. Gallagher *et al* [17] carried out microhardness indentation experiments on β-HMX, and identified the preferred slip planes as (001) and (101). They inferred that the likely slip systems were (001)[100], (101)[10$\bar{1}$] and (101)[010]. Dick *et al* studied the elastic plastic shock response of HMX crystals via plate impact experiments, and found that (010) shocks had larger elastic precursors than the {110} and {011} shocks [18]. This was explained by the fact that {110} and {011} shocks can produce plastic deformation via twinning and slip on the (101) and (001) planes, while {010} shocks did not lead to apparent plasticity. Barton *et al* [19] used molecular simulations to identify seven slip systems (in $P2_1/n$ space group): (010)[100], {011}[100], {011}[11$\bar{1}$], (101)[010], (101)[10$\bar{1}$], (001)[100], and (110)[001]. These were implemented in a crystal plasticity model to study hotspots and pore collapse under shock loading of single crystals.

This work is the first to systematically study dislocation stability and critical stresses in β-HMX using computational methods. First, we introduce a procedure to estimate the degree of steric hindrance during slip in various slip systems. This procedure is used to produce a preliminary ranking of the most active slip systems. Further, we use molecular simulations to estimate the Peierls–Nabarro (PN) stress, τ_{PN}, for dislocation motion in the slip systems with lowest degree of steric hindrance. This information is then used to determine whether there are enough slip systems in this material to accommodate a general state of plastic strain.

2. Models and procedures

β-HMX has a $P2_1/n$ monoclinic unit cell (or $P2_1/c$ [20]) with $\mathbf{a} = 6.5347$ Å, $\mathbf{b} = 11.0296$ Å, $\mathbf{c} = 7.3549$ Å, $\boldsymbol{\beta} = 102.689°$ and $Z = 2$ molecules per cell, as obtained by diffraction experiments performed at room temperature (295 K) [21, 22]. Atomistic simulations with the Smith–Bharadwaj (SB) potential at 295 K [23], lead to the lattice constants $\mathbf{a} = 6.58$ Å (+0.69%), $\mathbf{b} = 10.45$ Å (−5.25%), $\mathbf{c} = 7.67$ Å (+4.28%), $\boldsymbol{\beta} = 98.6°$ (−3.98%) in

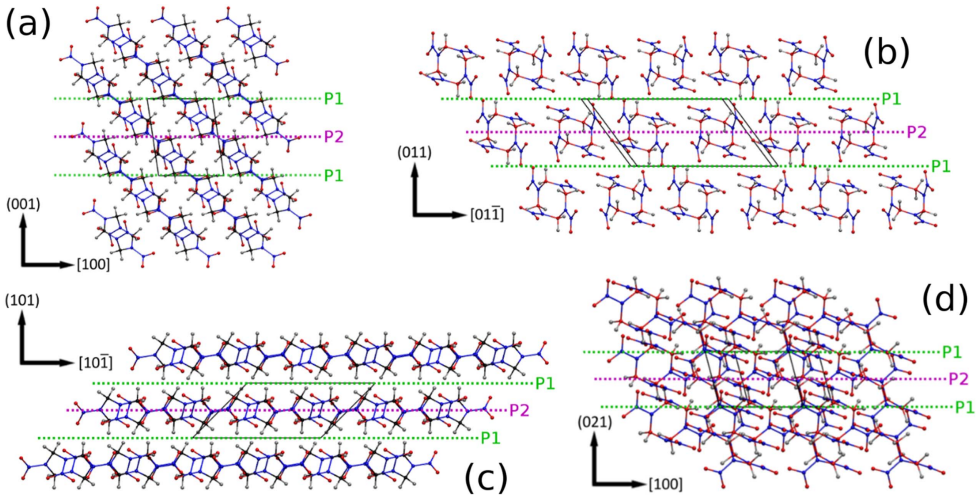

Figure 1. Several low index planes in β-HMX, with potential of being slip planes: (a) (001), (b) (011), (c) (101) and (d) (021). The P1 plane is considered for slip for all slip systems indicated, as it has equal or less steric hindrance compared to P2. The horizontal axis is along a slip direction, while the vertical axis is the slip plane normal (reciprocal coordinates). The (001) and (101) systems have been proposed in the literature [17] as potential slip planes.

reasonable agreement with experimental values (the deviation from experimental values are given in parentheses). Simulations at 0 K using the same potential produce slightly different lattice parameters $\mathbf{a} = 6.54$ Å, $\mathbf{b} = 10.25$ Å, $\mathbf{c} = 7.60$ Å and $\boldsymbol{\beta} = 98.51°$.

Some of the low index planes with potential of being slip planes are indicated in figure 1. Since there are two molecules per unit cell, two distinct parallel slip planes are available in general for each crystal plane; these are labeled P1 and P2 in figure 1. For the (001) plane, P1 and P2 are equivalent. For the (101) and (011), the P1 plane is less sterically hindered and therefore more likely to slip than P2. For the (021) plane, P1 and P2 are relatively similar but, based on similar topological considerations, P1 is more likely to slip.

Figure 2 shows the projection of the β-HMX unit cell in the frame of various slip systems considered in this study. Specifically, in figure 2 the slip plane normal is aligned with the vertical axis (z-axis) and dislocations move in the horizontal direction (x-axis). The sign of the applied shear stress is defined in the present discussion relative to these coordinate systems and directions.

In principle, many more slip systems can be considered as potential carriers of plasticity. Since the determination of the PN stress by atomistic simulations is computationally expensive, it is necessary to develop a preliminary ranking of slip systems that present the largest potential to be active. The classical way of addressing this problem requires selecting systems with large interplanar spacing (a_{hkl}) and shortest lattice vectors in the respective plane, or potential Burgers vectors (b_{mnp}). Here, hkl represents the index of the plane and mnp represents the direction of the Burgers vector. Large values of the a_{hkl}/b_{mnp} ratio indicate propensity to slip. This usually works well in monoatomic systems such as bcc and fcc metals [24]. In molecular crystals, this procedure may not be optimal owing to the complex geometry of the molecules and their packing.

Table 1 shows several slip systems cited in the literature for monoclinic β-HMX, ranked in the order of a_{hkl}/b_{mnp}. We observe that the slip systems observed experimentally [17],

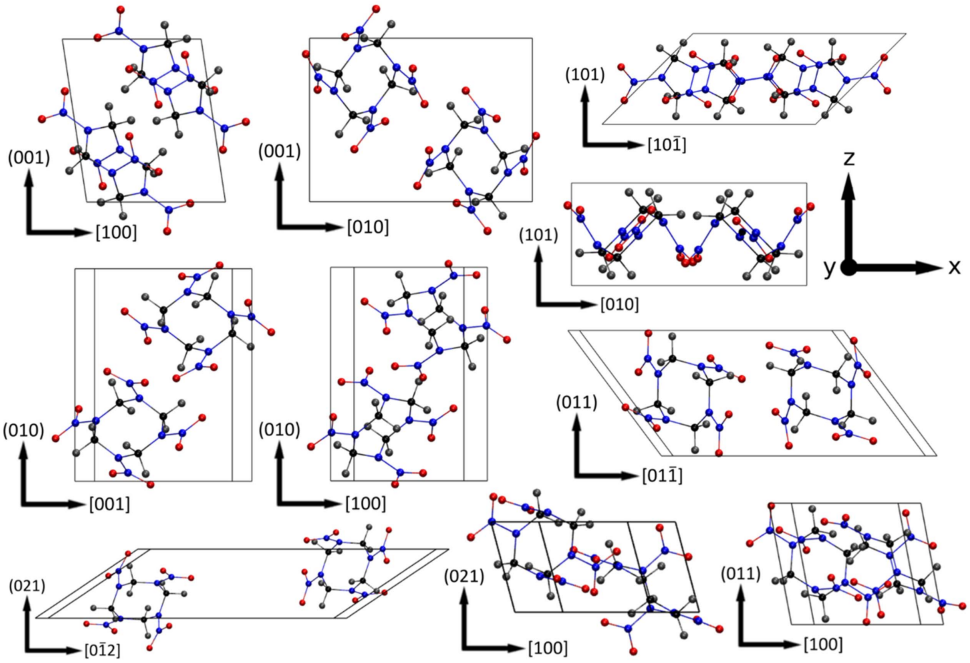

Figure 2. Projections of the β-HMX unit cell in the frame aligned with the slip plane normal (z-axis) and direction of dislocation motion (x-axis), for various slip systems considered in this study. A positive applied shear stress produces dislocation motion in the positive x-direction. The Burgers vector, indicating the direction of relative slip across the slip plane, can be oriented either in the direction of the x-axis, or in some other direction in the slip plane.

Table 1. Low index slip systems ranked in decreasing order of the ratio of interplanar spacing to the Burgers vector length (a_{hkl}/b_{mnp}). The (011) planes, which are symmetrically equivalent to (01$\bar{1}$), have the largest interplanar spacing and have the largest a_{hkl}/b_{mnp}. The commonly reported slip systems, (001)[100], (101)[10$\bar{1}$] and (101)[010] (shown in bold) are ranked poorly by this method. The values in the table are computed using lattice constants from diffraction experiments performed at room temperature [22]. Given the packing considerations discussed in figure 2, the relevant interplanar spacing for the (001) plane is $a_{hkl} = a_{002} = 3.588$ Å, while for the (010) plane, $a_{hkl} = a_{020} = 5.515$ Å.

System $(hkl)[mnp]$	a_{hkl}/b_{mnp}	System $(hkl)[mnp]$	a_{hkl}/b_{mnp}
(011)[100]	0.920	(**001**)[**100**]	**0.549**
(010)[100]	0.844	(10$\bar{1}$)[010]	0.489
(010)[001]	0.750	(011)[01$\bar{1}$]	0.454
(110)[001]	0.750	(110)[1$\bar{1}$0]	0.431
(021)[100]	0.669	(12$\bar{1}$)[101]	0.443
(10$\bar{1}$)[101]	0.620	(**101**)[**10$\bar{1}$**]	**0.398**
(120)[001]	0.567	(**101**)[**010**]	**0.391**
(11$\bar{1}$)[101]	0.557		

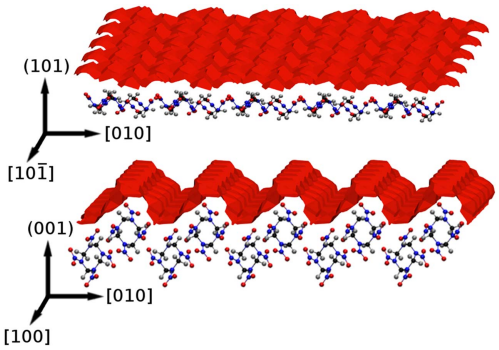

Figure 3. Slip surfaces for (101) and (001) planes. The (101) surface has smaller protrusions and the degree of overlap associated with slip in any in-plane direction is small. This is not the case for the (001) plane for which the overlap associated with sliding in the [010] direction is more pronounced than that associated with slip in the [100] direction. The periodicity of the 'ridges' of the (001) plane in the [010] direction is 10.25 Å, which corresponds to the lattice periodicity in this crystal direction. The amplitude in the direction perpendicular to the plane is 2.8 times larger in the (001) case compared with the (101) case. The molecular structure of the respective planes is shown below each of the two slip surfaces. The continuous surface is the envelope of the molecular structure.

(001)[100], (101)[10$\bar{1}$] and (101)[010], are ranked poorly by this custom. This raises doubts about the usefulness of the standard procedure in the case of molecular crystals.

Thus, a more reliable method that can be used to rank slip systems more accurately in molecular crystals is needed. We propose a new identification method based on the degree of steric hindrance or geometric overlap during slip. For given slip system, we consider the geometry of the slip surface and compute a geometrical γ-surface based on the topological overlap of molecules associated with relative rigid body motion across the respective slip plane. To avoid confusion with the usual γ-surface, we denote these geometric γ-surfaces as 'g-surfaces.' The procedure requires defining first objects corresponding to individual molecules. To this end, a Voronoi tessellation of the atoms in the molecular crystal is created based on van der Waals radii of the atoms. The Voronoi cells are then grouped according to the molecule they belong to and the shape of such a group reflects the volume occupied by the molecule. This geometric representation of individual molecules is used to construct entire slip surfaces, as shown in figure 3 for the (101) and (001) crystal planes of β-HMX. On both sides of the slip surface, the Voronoi cell groups form crystalline clusters. In the initial state, the clusters on opposite side of the glide plane match perfectly and there is no overlap. Following the usual procedure of finding the γ-surface [25], the two clusters across a given glide plane are tangentially displaced relative to each other while preserving their relative distance in the direction perpendicular to the slip plane. The volumetric overlap of the Voronoi clusters is determined and used as an estimate of the steric hindrance during slip.

The definition used here for the volume of a molecule is somewhat related to the procedure based on the Hirshfeld surface. Hu *et al* used the Hirshfeld partition to quantify molecular packing in various crystal directions, which they related to steric hindrance and subsequently, to impact sensitivity [26].

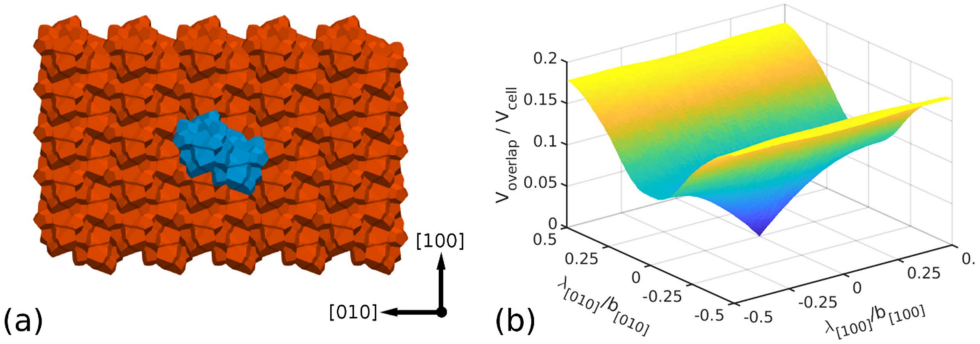

Figure 4. (a) (001) Slip surface (red) and unit cell of the crystal layer above it (blue). Moving the blue solid horizontally, in the (001) plane, in two directions results in steric overlap between the red and blue solids. The volume of this overlap provides the geometric g-surface shown in (b). The horizontal axes are normalized by the lattice periodicity in the respective directions, specifically, the [100] axis is normalized by $b_{[100]} = 6.54$ Å, and the [010] axis is normalized by $b_{[010]} = 10.25$ Å. The vertical axis is normalized by the unit cell volume ($V_{\text{cell}} = 504$ Å^3).

The slip surfaces provide qualitative indication as to which slip directions are likely. For example, the (001) surface indicates that slip along [100], i.e. parallel to the 'ridges' in figure 3, is much more likely than along [010]. For the (101) surface, slip along both low index directions contained in the respective plane, i.e. $[10\bar{1}]$ and [010] is possible. This is in agreement with a suggestion by Gallagher *et al* [17]. The degree of overlap corresponding to a specific relative shift can be used to make this prediction more quantitative. Figure 4(a) shows the top view of the (001) surface with one cell (representing a molecule) of the opposing crystal surface represented in blue. The blue unit is shifted in arbitrary directions parallel to the (001) plane. The resulting overlap normalized by the unit cell volume ($V_{\text{cell}} = 504$ Å^3) is shown in figure 4(b).

This procedure provides only an approximate idea about the nature of slip since energetic interactions are not considered. To obtain a definitive ranking of slip systems, the critical stress for dislocation motion, i.e. the PN stress [24, 27], has to be evaluated. The PN stress is computed using an atomistic model of a dislocation dipole in a large crystal domain with periodic boundary conditions. The dipole is introduced in the model by displacing the centers of mass (COMs) of all molecules according to the isotropic Volterra field and providing a final rigid rotation to the system to correct the spurious error induced by the conditionally convergent summation of the contribution of images [28]. This method is similar to that used to calculate PN stresses in RDX [29].

A schematic representation of the model used to estimate the PN stress is shown in figure 5. Edge dislocations of opposite signs are placed at ($x = 0.25\ L_X$, $z = 0.25\ L_Z$) and ($x = 0.75\ L_X$, $z = 0.75\ L_Z$) (figure 5(a)). Screw dislocations of opposite signs are placed at ($x = 0.5\ L_X$, $z = 0.25\ L_Z$) and ($x = 0.5\ L_X$, $z = 0.75\ L_Z$) as shown in figure 5(b)). In this configuration, the dislocations are in equilibrium with all neighbors and the net force acting on them vanishes. The system is subsequently relaxed at 0 K and 0 atm. using isothermal–isostress ($N\sigma T$) ensemble integrators [30]. The size of the model ($N_x \times N_y \times N_z$ unit cells) in the two directions in the plane x–z of figure 5 is selected such that 370 Å $< L_x, L_z <$ 380 Å in

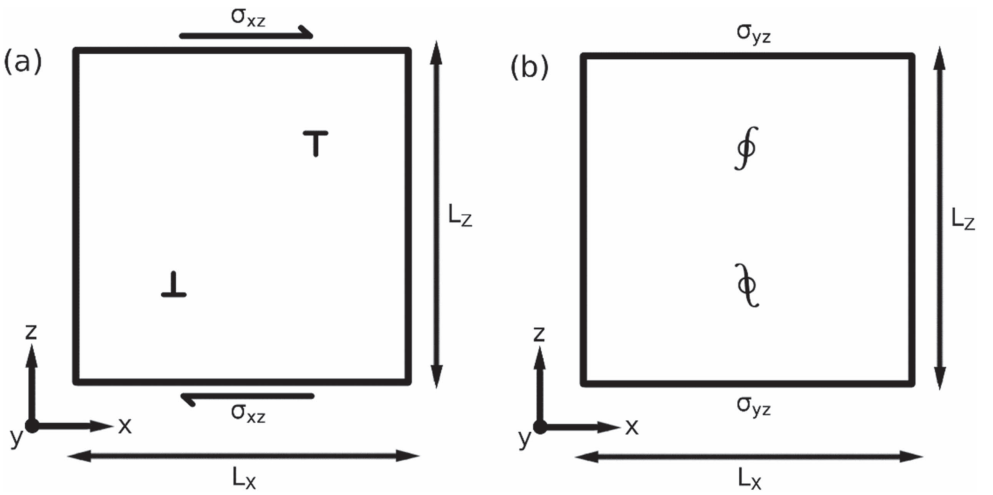

Figure 5. Dislocation dipole setup (for edge (a) and screw (b) dislocations) used to compute PN stresses. The positions of edge dislocations are indicated by $\perp$ while screw dislocations are indicated by $\oint$. The glide plane is normal to the z-axis. The Burgers vector is along the x-axis for edge dislocations and along the dislocation line (which may or may not be aligned with the y-axis) for screw dislocations. The applied stress for glide is σ_{xz} and σ_{yz} for edge and screw dislocations, respectively. Dislocations move in the x-direction in all cases.

all cases. The model dimension in the y-direction in figure 5 is kept small ($N_y = 1$). This forces the dislocation line to remain straight during motion. Increasing values of the resolved shear stress (σ_{xz} or σ_{yz}) are applied using the same ensemble ($N\sigma T$) at 10^{-4} K and the minimum stress that leads to dislocation motion is recorded. The temperature is kept finite (but very close to 0 K) to assist the relaxation procedure.

The force field used for all models is the SB potential [23], which was developed using quantum chemistry calculations to reproduce structural properties for HMX and dimethyl dinitro methyldiamine. This potential was modified by scaling partial atomic charges by 25% [31], to reproduce condense phase density and cohesive energy and is the one used in this work. This potential reproduces experimental lattice constants, thermal expansion coefficients, heats of sublimation [31], elastic constants [32], phase transitions [33], thermal conductivity [34], melting [35] and sublimation enthalpy [36] in HMX.

Voronoi tessellations are performed using the Voro++ software package [37], and unit cells of β-HMX are obtained in various crystallographic systems using the GCCM package [38]. The volumetric overlap is computed using Libigl [39] boolean mesh operations after converting the Voronoi assemblies to stereolithography meshes via a custom code. Images of the slip surfaces are rendered in Paraview [40]. All molecular simulations are performed with LAMMPS (16 Feb 2016 version) [41]. The long-range Coulombic interactions were computed in reciprocal K-space by a particle–particle particle-mesh solver with relative force error of 10^{-4}. The pair-wise interactions were cut-off at 15 Å. Input scripts and unit cell data are provided in the supplementary information available online at stacks.iop.org/MSMS/26/045005/mmedia.

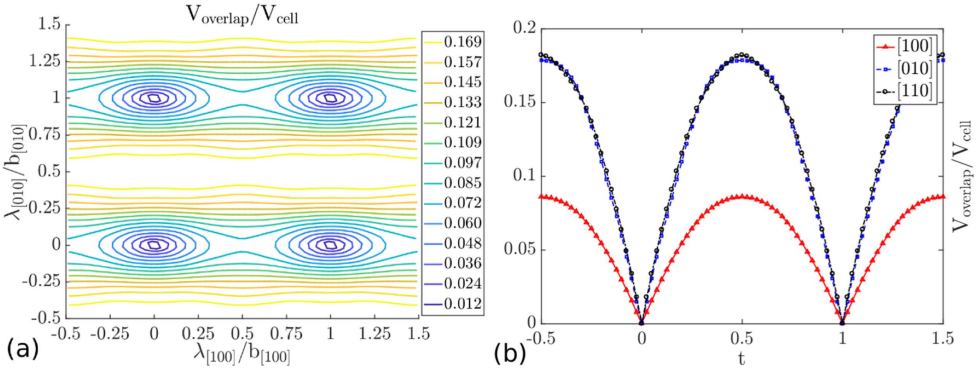

Figure 6. (a) Contour map of the normalized g-surface for the (001) P1 plane. The horizontal and vertical axes are normalized by 6.54 Å and 10.25 Å, respectively. The values of the map are normalized by V_{cell}. (b) Line projections of the g-surface in (a) along [100], [010], and [110]. t represents the coordinate in the respective direction normalized by the periodicity in that direction.

3. Results

3.1. Geometric g-surfaces

As discussed above, we construct g-surfaces in order to rank slip systems in terms of the steric hindrance associated with slip. This method considers the geometry of molecules and their packing and hence incorporates more information than the simple estimate based on a_{hkl}/b_{mnp} (table 1). This method is applied to all major slip system candidates and leads to a preliminary ranking of slip systems. This allows reducing the number of systems for which the much more expensive atomistic PN calculations are performed. The g-surfaces for the major slip planes are presented in this section.

3.1.1. (001) plane. The (001)[100] system was suggested by Gallagher *et al* [17] based on indentation experiments to be among the prominent candidates for slip. The normalized g-surface for the (001) plane is shown in figure 6(a) and values are normalized with V_{cell}. It has a saddle point of magnitude 0.084 V_{cell} when sampled along the [100] direction, and a saddle of magnitude 0.179 V_{cell} when sampled along the [010] direction. This indicates that the steric hindrance for slip along [100] is much lower than that for slip along [010] (figure 6(b)). Thus, slip is more likely to happen in this plane in the [100] direction, which is consistent with Gallagher's suggestion. The lack of minima at positions other than those corresponding to the lattice periodicity (see e.g. the [110] trace in figure 6(b)) indicate that the formation of partial dislocations is unlikely.

3.1.2. (101) plane. Experiments by Gallagher *et al* [17] also indicate that slip is likely along (101)[10$\bar{1}$] and is possible along (101)[010]. The normalized g-surface for the (101) plane is shown in figure 7(a). The surface is relatively flat compared to that for the (001) plane (figure 6). The maximum values of the normalized overlap for relative sliding along [10$\bar{1}$] and [010] are 0.048 and 0.069, respectively (figure 7(b)). These values are low compared to those for the (001)[100] system (figure 6), and slip may occur in both low index directions in this plane. This conclusion agrees with experimental findings. Formation of partials is unlikely as the minima close to the center of the field in figure 7(a) are relatively shallow.

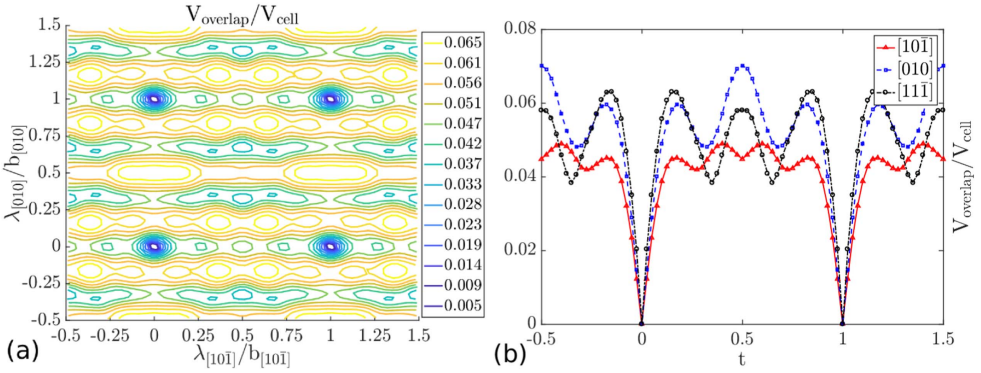

Figure 7. (a) Contour map of the normalized g-surface for the (101) P1 plane. The horizontal and vertical axes are normalized by 10.73 Å and 10.25 Å respectively. The values of the map are normalized by V_{cell}. (b) Line projections of the g-surface in (a) along $[10\bar{1}]$, [010], and $[11\bar{1}]$. t represents the coordinate in the respective direction normalized by the periodicity in that direction.

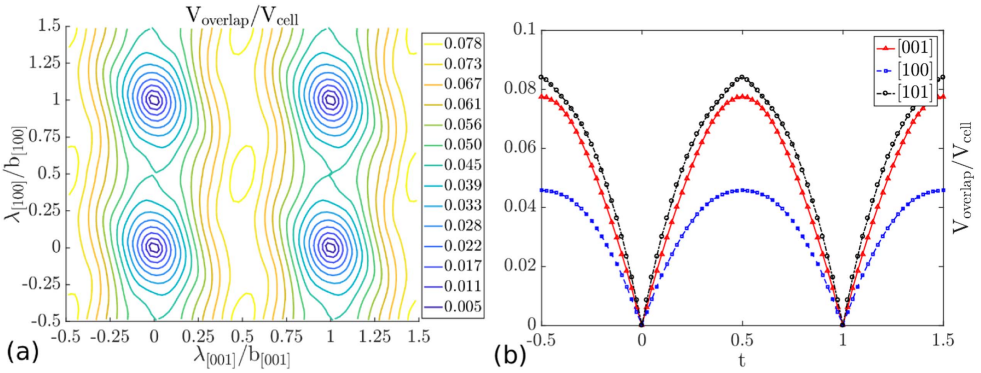

Figure 8. (a) Contour map of the g-surface for the (010) P1 plane. The horizontal and vertical axes are normalized by 7.60 Å and 6.54 Å respectively. The values of the map are normalized by V_{cell}. (b) Line projections of the g-surface in (a) along [001], [100], and [101]. t represents the coordinate in the respective direction normalized by the periodicity in that direction.

3.1.3. (010) *plane.* The normalized g-surface for the (010) plane is shown in figure 8(a). The saddle point along [100] is 0.045 V_{cell}, lower than that along [001], which in 0.076 V_{cell} (figure 8(b)). This suggests that slip along both directions is possible, and that [100] is the easier glide direction. A maximum in the central region of the map of figure 8(a) suggests that, once again, the formation of partials in this slip system is unlikely.

3.1.4. (011) *plane.* The normalized g-surface for the (011) plane is shown in figure 9(a). This map exhibits interesting features. There is a well comprising two minima in the central region of the map in figure 9(a), which suggests that partials may form in this slip system. The low values of the maximum normalized overlap along [100] and $[01\bar{1}]$ (0.084 V_{cell} and 0.078 V_{cell}, respectively, figure 9(b)) suggest that slip in both directions is likely. It is important to note that this plane was reported as a cleavage plane in [14].

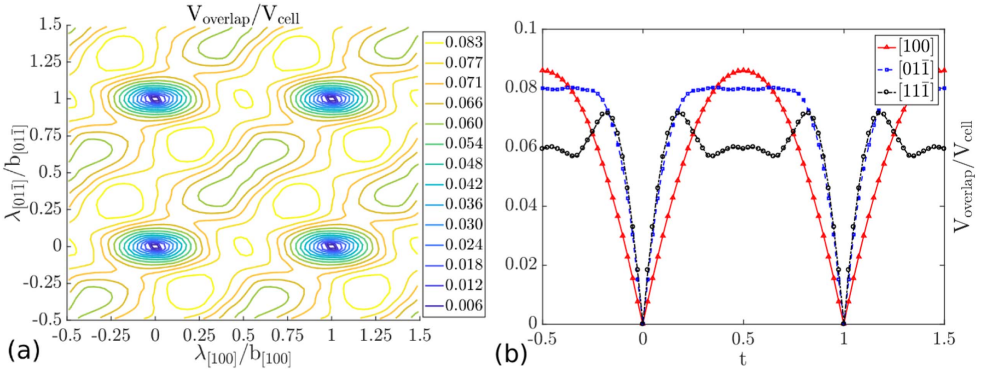

Figure 9. (a) Contour map of the normalized g-surface for the (011) P1 plane. The horizontal and vertical axes are normalized by 6.54 Å and 12.76 Å respectively. The values of the map are normalized by V_{cell}. (b) Line projections of the g-surface in (a) along [100], [01$\bar{1}$], and [11$\bar{1}$]. t represents the coordinate in the respective direction normalized by the periodicity in that direction.

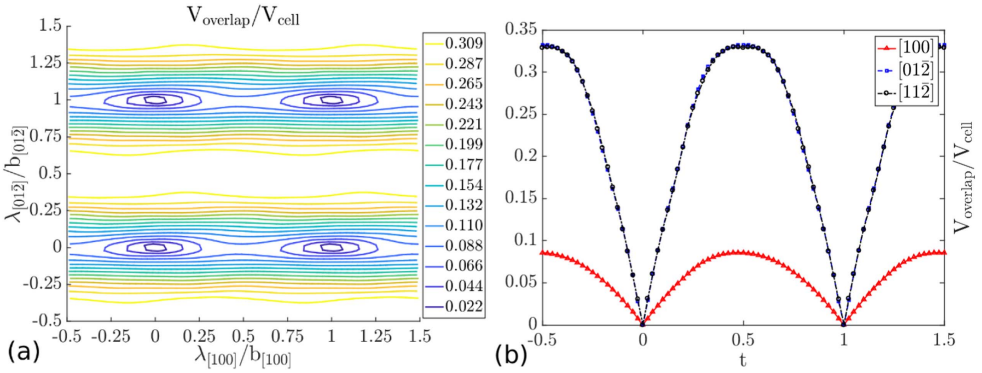

Figure 10. (a) Contour map for the g-surface for the (021) P1 plane. The horizontal and vertical axes are normalized by 6.54 Å and 18.33 Å respectively. The values of the map are normalized by V_{cell}. (b) Line projections of the g-surface in (a) along [100], [01$\bar{2}$], and [11$\bar{2}$]. t represents the coordinate in the respective direction normalized by the periodicity in that direction.

3.1.5. (021) *plane.* The normalized g-surface for the (021) plane is shown in figure 10(a). This surface is similar to that corresponding to the (001) plane (figure 6). The saddle point for the low overlap [100] direction has a value of 0.084 V_{cell} which is low enough to warrant slip along [100]. Thus, slip is more likely to happen in this plane along [100] than along [01$\bar{2}$], for which the maximum normalized overlap is large, 0.325 (figure 10(b)). The absence of other minima on the g-surface indicates that partial formation is unlikely.

3.1.6. Summary of the g-surface analysis. Geometric g-surfaces for several other low index slip planes (11 planes and 22 systems in total) are constructed and the results are presented in table 2. The g-surfaces provide information related to the steric hindrance during slip. This analysis needs to be supplemented with information related to the energy per unit length of the dislocation line. Since the system tends to minimize the total stored strain energy, only

Table 2. Ranking of low index slip systems in terms of the composite parameter, $K_{\text{aniso}}(V_{\text{overlap}}/V_{\text{cell}})$, representing the normalized steric overlap ($V_{\text{overlap}}/V_{\text{cell}}$) and the strain energy per unit length of dislocation line (proportional to K_{aniso}). Entries shown in bold indicate slip systems inferred based on experimental observations [17]. The shaded region of the table indicates slip systems for which PN stress calculations are performed. For the (011) plane, the partial system $\frac{1}{2}(011)[01\bar{1}]$ is included since the g-surface provides evidence for partial formation. Elastic constants used for computing K_{aniso} are provided.

Plane type	Plane	Direction	$V_{\text{overlap}}/V_{\text{cell}}$	K_{aniso} (10^{-9} J m^{-1})	$K_{\text{aniso}}(V_{\text{overlap}}/V_{\text{cell}})$ (10^{-9} J m^{-1})
P1	(010)	[100]	0.045	0.3401	0.0152
P1	(**001**)	[**100**]	0.084	0.3407	0.0286
P1	(011)	½[01$\bar{1}$]	0.078	0.3615	0.0283
P1	(021)	[100]	0.084	0.3557	0.0299
P1	(011)	[100]	0.084	0.3569	0.0300
P1	(010)	[001]	0.076	0.4893	0.0371
P1	(**101**)	[**10$\bar{1}$**]	0.048	0.9394	0.0450
P1	(**101**)	[**010**]	0.069	0.9009	0.0618
P1	(100)	[001]	0.137	0.4597	0.0628
P1	(110)	[001]	0.137	0.4660	0.0637
P1	(120)	[001]	0.139	0.4735	0.0658
P1	(10$\bar{1}$)	[010]	0.069	0.9737	0.0668
P1	(011)	[01$\bar{1}$]	0.078	1.4459	0.1134
P2	(111)	[10$\bar{1}$]	0.125	0.9396	0.1177
P1	(001)	[010]	0.175	0.8373	0.1463
P1	(100)	[010]	0.179	0.8226	0.1474
P1	(110)	[1$\bar{1}$0]	0.139	1.3164	0.1835
P1	(11$\bar{1}$)	[101]	0.375	0.6532	0.2450
P1	(10$\bar{1}$)	[101]	0.456	0.6834	0.3119
P2	(111)	[1$\bar{1}$0]	0.250	1.2718	0.3180
P1	(11$\bar{1}$)	[1$\bar{1}$0]	0.269	1.3956	0.3753
P1	(120)	[2$\bar{1}$0]	0.325	2.4952	0.8109
P1	(021)	[01$\bar{2}$]	0.325	2.7371	0.8904

Note. Elastic constants [32] used for computing the pre-logarithmic factor K_{aniso}: $C_{11} = 22.2$, $C_{22} = 23.9$, $C_{33} = 23.4$, $C_{44} = 9.2$, $C_{55} = 11.1$, $C_{66} = 10.1$, $C_{12} = 9.6$, $C_{13} = 13.2$, $C_{23} = 13.0$, $C_{15} = -0.1$, $C_{25} = 4.7$, $C_{35} = 1.6$, $C_{46} = 2.5$ (GPa).

dislocations of lowest energy per unit length of the dislocation line can be stabilized. This specific energy is quantified using the pre-logarithmic factor of the dislocation strain energy computed in anisotropic elasticity, $K_{\text{aniso}} = K_{mg} b_m b_g$, where K_{mg} is the pre-logarithmic energy tensor and **b** is the Burgers vector [42]. We combine this energetic parameter with that resulting from the overlap analysis and use the product $K_{\text{aniso}}(V_{\text{overlap}}/V_{\text{cell}})$ to generate a ranking of slip systems. A low value for this combined parameter for a slip system indicates higher likelihood that dislocations can be stabilized and can glide in the respective system.

Table 2 shows the values of these parameters for all systems considered in the study. The experimentally suggested slip systems, (001)[100], (101)[10$\bar{1}$] and (101)[010], are shown in bold. The new criterion performs better than that used in the ranking of table 1; all experimentally observed slip systems are among the top 8 in this ranking. System (001)[100] moves from position 9 in table 1 to position 2.

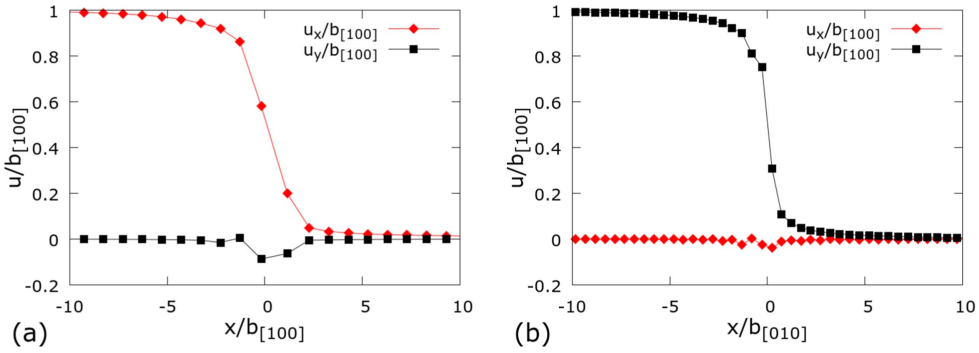

Figure 11. Burgers profile for (a) edge dislocations and (b) screw dislocations in the (001)[100] system. The axes are normalized by $b_{[100]}$ and $b_{[010]}$, with $b_{[100]} = 6.54$ Å and $b_{[010]} = 10.25$ Å.

Since the overlap analysis does not incorporate detailed energetics and does not account for molecular flexibility and the finite width of dislocations, its results can be only considered qualitative. This underlines the need for atomistic PN stress calculations. We select the top eight systems in table 2 for this purpose. We aim to identify a sufficient number of systems that can accommodate a generic plastic strain. Further, the largest PN stress value among all these systems indicates the level of global stress needed to produce generic plasticity in this material.

3.2. Peierls–Nabarro stresses

Dislocations are setup and relaxed according to the procedure outlined in section 2. Here we discuss the Burgers profiles and present the PN stresses for dislocations in selected slip systems (shaded area of table 2). The core profiles are evaluated using the standard procedure [43], by calculating the relative displacement of molecular COMs across the respective glide plane ($u_x(x)$, $u_y(x)$), with directions x and y defined in figure 5. An arctan function of the form $u(x) = b \tan^{-1}((x - x_0)/w)$ is fit to $u_x(x)$ (or $u_y(x)$) such to infer the width of the dislocation core (w). Here b represents the magnitude of the Burgers vector in the respective system. Generally, a core of smaller width is expected to have a higher PN stress than a core of larger width [27].

The dislocation setup is relaxed at 0 K using molecular simulations and the core is deemed to be stable if no cleavage is observed and if the core does not cross-slip to a different crystal plane. The dislocation is then loaded by applying a shear stress on the boundary of the model, and the stress at which the dislocation moves is recorded as the PN stress. In some cases, cleavage starting from the core is observed under stress or the dislocation cross-slips instead of steadily moving along the desired glide plane. This occurs when the crystal accommodates the applied shear stress by adopting a different configuration, incompatible with slip. Such cases are labeled ‘unstable’ in the present discussion.

3.2.1. Dislocation stability and Burgers profiles. For most slip systems considered, the core is narrow and does not split into partials. This confirms the expectations based on the g-surface analysis. The Burgers profiles for the (001)[100] edge and (001)[100] screw dislocations are shown in figure 11. These profiles are typical of most of the slip systems considered. The

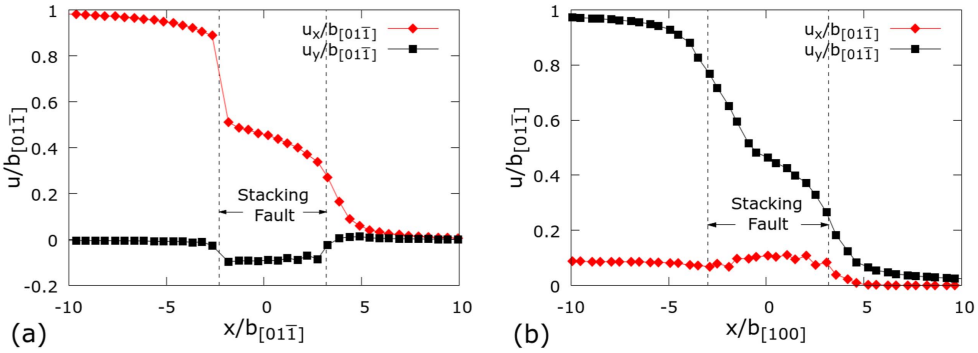

Figure 12. Burgers profile for (a) edge dislocations and (b) screw dislocations in the (011)[01$\bar{1}$] system. The axes are normalized by the length of the Burgers vectors indicated, with $b_{[01\bar{1}]} = 12.76$ Å and $b_{[100]} = 6.54$ Å. Both edge and screw dislocations split into partials of roughly equal Burgers vectors. The position of the partials is indicated with vertical lines which also mark the spatial extent of the stacking fault.

Table 3. Core widths for stable dislocations in select slip systems. The values marked by * indicate widths of partials.

Plane [*hkl*]	Burgers [*mnp*]	Edge core width (Å)	Screw core width (Å)
(010)	[100]	3.39	5.33
(010)	[001]	3.37	4.95
(101)	[010]	13.29	7.78
(101)	[10$\bar{1}$]	5.01	8.28
(011)	[100]	5.84	3.92
(011)	[01$\bar{1}$]	4.30, 8.42*	7.27, 5.60*
(001)	[100]	4.15	3.53
(021)	[100]	4.32	2.77

cores are narrow, with a width of 4.15 Å and 3.53 Å respectively and exhibit minimal distortion in the direction perpendicular to the Burgers vector.

A notable exception is the core profile for edge and screw dislocations in the (011)[01$\bar{1}$] system (figure 12). This core splits into partials of width 4.3 Å, 8.42 Å for edges and 7.27 Å, 5.6 Å for screw, separated by a stacking fault. Note that the distance between the two partials is small, which indicates that the corresponding staking fault energy is large. This can be understood from the framework of the (011) g-surface (figure 9), which exhibits a well in the center of the field. Each partial has edge and screw components. For the edge dislocation case, the net Burgers vector is in the [01$\bar{1}$] direction (along the *x*-axis), and the partials have equal edge and screw components. The screw component of these partials is $\pm 0.1^* b_{[01\bar{1}]}$ (figure 12(a)). For the screw dislocation (figure 12(b)), the Burgers vector is oriented in the [01$\bar{1}$] direction, along the dislocation line. Therefore, the Burgers vector is not perpendicular to the *x*-axis or to the glide direction. This specific orientation renders $u_x \neq 0$ and $u_y < 1$ at the left end of figure 12(b). The width of all stable cores is reported in table 3.

3.2.2. Peierls–Nabarro stress. The PN stress is the minimum stress required to move an isolated dislocation in the absence of thermal activation at 0 K. This threshold stress is computed for all slip systems in the shaded area of table 2.

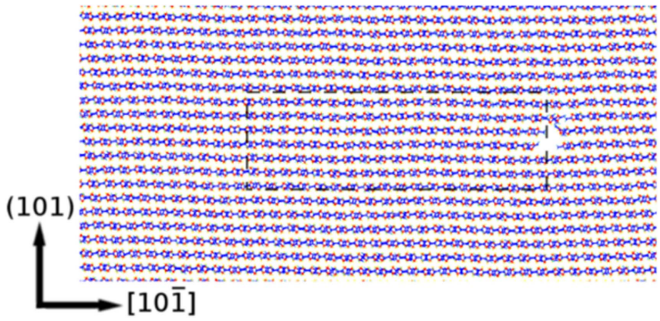

Figure 13. Core structure for the (101)[10$\bar{1}$] edge dislocation. A locally twinned region forms to the left of the core, which appears as a gap after relaxation. This local twin elongates away from the core (to the left in this image) on application of positive shear stress, and shrinks, eventually closing the gap and slipping via dislocation motion, when the direction of stress is reversed.

For the (001) plane, (001)[100] edge and screw dislocations are considered. The edge dislocation is stable in the absence of an applied stress and moves at a minimum stress of −0.47 GPa. The application of a positive resolved shear stress (relative to the coordinate system in figure 2) causes the dislocation to become unstable leading to cleavage along the (101) plane. Therefore, slip in the positive direction is not possible. The screw dislocation core is also stable in the absence of far field stress and moves under an applied stress of 0.55 GPa. When the direction of stress is reversed, the dislocation splits into two identical screw dislocations that cross-slip along (011) and (01$\bar{1}$) planes, respectively. Thus, screw and edge dislocations glide asymmetrically, in opposite directions.

For the (101) plane we consider two slip directions: [010] and [10$\bar{1}$]. For the (101)[010] system, the edge dislocation moves under a minimum applied stress of −0.26 and 0.28 GPa in the two directions of the x-axis (figure 2), while the screw dislocation moves under minimum applied stresses of −0.12 GPa and 0.11 GPa, respectively, indicating that this slip system is likely to be active. This is consistent with conclusions obtained by Gallagher *et al* [17]. In the unloaded state, the core of the edge dislocation in this system acquires a screw component, but the separation between partials is small. As the core moves, the partials become better defined. This indicates that the γ-surface for the (101) plane has a minimum corresponding to a stable stacking fault, although the g-surface for this plane (figure 7) does not show such distinct minimum.

For the (101)[10$\bar{1}$] system, the behavior is quite different for edge and screw dislocations. For edge dislocations, the core relaxes to form a twin of limited extent as shown in figure 13. Upon application of positive shear stress in the frame of figure 13, the length of the twin increases. Upon application of negative shear stress, the twin length decreases, the core becomes compact (undissociated) and further dislocation slip is observed (the dislocation moves to the right, figure 13). Clearly this behavior cannot be explained entirely by edge dislocation motion, and hence computation of PN stresses for this system is not meaningful. This is in agreement with experimental observations which indicate that (101) is twinning composition plane [15]. For screw dislocations, slip is observed in both directions, but the PN stress is asymmetric, i.e. −0.39 GPa and 0.13 GPa in the negative and positive directions of the x-axis (figure 2), respectively.

The g-surface analysis indicates that slip is likely to occur in the (010) plane along the [100] direction (table 2). However, the atomistic analysis leads to a different conclusion. It is

observed that edge dislocation cores are stable if no far field is applied but become unstable leading to cleavage along $(1\bar{1}0)$ and (110) planes once either a positive or negative resolved shear stress is applied. Screw dislocations, which have stable narrow cores in the unloaded state, cross-slip to the $(01\bar{1})$ and (011) planes upon shear loading in the negative and positive directions, respectively.

For the (010)[001] system, edge dislocation cores are stable at zero applied stress, but produce cleavage along $(01\bar{1})$ and (011) upon negative and positive shear loading, respectively. For screw dislocations in this system, extended defect domains are seen near the core when load is applied, while the dislocation remains stationary. These domains comprise molecules that are rotated and distorted relative to the perfect crystal configuration. Thus, this system is found to be unsuitable for slip. This emphasizes again the limitations of the excluded-volume based geometric g-surfaces.

The (021) g-surface indicates that slip is likely only along [100] (figure 10). Edge dislocations in the (021)[100] slip system are mobile, with the PN stresses in the two directions of the respective crystal axis being −0.43 and 0.51 GPa. Screw dislocations in this system are stable in the absence of stress, but cross-slip along (011) planes upon shear loading in either direction.

The g-surface and unloaded core profile analyses for the (011) plane indicates that partials may form when the Burgers vector is oriented in the $[01\bar{1}]$ direction. The PN stress computed for the $(011)[01\bar{1}]$ edge system is 0.4 GPa. This is the stress required to move the entire dislocation. The partials are identical and move at the same critical stress. For the reverse loading direction, the partials collapse, and the dislocation becomes unstable, leading to cleavage along $(01\bar{1})$. For the screw dislocation in the $(011)[01\bar{1}]$ slip system, glide is observed once the applied resolved shear stress exceeds −0.05 and 0.12 GPa in the two directions of the $[01\bar{1}]$ axis. This dislocation is also split into partials (figure 12(b)). For the (011)[100] system, the compact edge dislocation core moves at a PN stress of −0.26 GPa. For positive shear stresses, the cores became unstable and cleavage is observed along the (111) plane. Screw dislocations on this system exhibit the largest PN stresses of all systems considered, i.e. −0.75 and 0.32 GPa in the two directions along [100].

Table 4 presents a summary of this discussion and the PN stresses computed for the various slip systems considered. The three systems reported by Gallagher *et al* [18] are shows in bold and are seen to be active either in slip, or slip and twinning. Three additional slip systems, namely $(011)[01\bar{1}]$, (011)[100] and (021)[100], are observed to be active and are reported in table 4.

It is important to underline that slip asymmetry is the norm for all systems considered. Slip asymmetry is unusual in FCC lattices, but is observed in BCC. However, the asymmetry in HMX is much more pronounced than in most other materials. Slip asymmetry was also observed in RDX [44] and was associated with the relative orientation of nitro groups of molecules across the glide plane. The asymmetry reported here is associated with both steric and energetic interactions and is significantly more pronounced than in RDX.

Most systems exhibit complex behavior, beyond slip asymmetry. Dislocations may be mobile in one direction but become unstable or cross-slip when loaded in the opposite direction. An interesting example is the (001)[100] slip system, in which we observe core instability, cross-slip and dislocation glide depending on the direction of loading. Likewise, edge and screw dislocations behave differently in any given system. These complexities are, to a large extent, a consequence of molecular packing (steric effects) and are nuanced by energetic interactions. Their presence makes developing coarse grained representations of slip in this molecular crystal quite a daunting task.

Table 4. Selected slip systems for β-HMX, their overlap values, and PN stresses. Both edge and screw dislocations are considered for each system and PN values are reported for the two possible loading directions (see figures 2 and 5 for the definition of the positive direction relative to the molecular orientation in the perfect crystal). Systems sustaining slip of at least one type of dislocation are highlighted in gray. Slip systems indicated in bold have been observed experimentally [17]. In the table, 'unstable' indicates that cleavage occurs upon loading starting from the dislocation core, 'twin' indicates that a twin nucleus forms upon relaxation of the core and this twin grows when the load is applied, 'twin and slip' indicates that the twin nucleus decreases in size and regular dislocation slip is observed when the load is applied in the respective direction. In the case labeled 'point defect domains', a domain of rotated and distorted molecules forms in the vicinity of the core upon loading and the core does not move.

Selected slip system			Edge dislocation		Screw dislocation	
Plane	Burgers direction	$K_{aniso}{}^{*}(V_{overlap}/V_{cell})$ $(10^{-9}\,J\,m^{-1})$	$\sigma_{xz} < 0$ (GPa)	$\sigma_{xz} >= 0$ (GPa)	$\sigma_{yz} < 0$ (GPa)	$\sigma_{yz} >= 0$ (GPa)
(010)	[100]	0.0152	Unstable	Unstable	Cross-slip on $(01\bar{1})$	Cross-slip on (011)
(**001**)	[**100**]	0.0286	−0.47	Unstable	Cross-slip on {011}	0.55
(011)	$[01\bar{1}]$	0.0283	Unstable	0.40	−0.05	0.12
(011)	[100]	0.0300	−0.26	Unstable	−0.75	0.32
(021)	[100]	0.0299	−0.42	0.5	Cross-slip on (011)	Cross-slip on (011)
(010)	[001]	0.0371	Unstable	Unstable	Point defect domains	
(**101**)	[**10$\bar{1}$**]	0.0450	Twin and slip	Twin	−0.39	0.13
(**101**)	[**010**]	0.0618	−0.26	0.28	−0.12	0.11

4. Discussion

A single crystal accommodates a generic plastic strain defined by six independent plastic strain components if it has five independent slip systems [45]. In order to determine whether β-HMX fulfills this condition, we adopt the procedure used by Groves and Kelly [46], and described in Hirth [43]. The slip systems discussed in section 3 exhibit complex behavior. In this analysis we consider a system to be active if either screw or edge dislocations exhibit bidirectional glide. We also include system (001)[100] in which bidirectional slip is accommodated by the combination of edge and screw dislocations. Thus, eight slip systems are selected (six are highlighted in table 4 and all eight are shown in table 5), which include the experimentally observed (001)[100], (101)[10$\bar{1}$] and (101)[010] systems, as well as the (021)[100] and four systems on the two equivalent {011} planes.

This analysis indicates that out of the 56 ($^8C_5$) combinations of groups of five slip systems considered, 22 combinations can accommodate general plastic strain. It is now possible to indicate the range of PN stress that needs to be applied for the activation of five independent slip systems. The systems with the lowest PN stress (in either positive or negative glide directions) are (101)[010], (101)[10$\bar{1}$], (011)[01$\bar{1}$] and (01$\bar{1}$)[011], which are all active once the respective resolved shear stress is equal to, or larger than 130 MPa. However, these systems are insufficient to accommodate an arbitrary plastic strain. The addition of the (011)[100] and (01$\bar{1}$)[100] systems leads to a set which allows for generalized slip, but this requires a minimum resolved shear stress of 260 MPa. It is important to note that the twinning system (101)[10$\bar{1}$] must be included in the list of active systems in all cases (table 5). Therefore, twinning is necessary in order for the crystal to accommodate a generalized plastic strain, a situation similar to HCP metals [47]. The analysis is approximate as it does not account for slip asymmetry and contrasting behaviors of edge and screw dislocations.

It is important to reconsider the limitations of this study. These results are exact (subject to model limitations) at 0 K. The threshold stresses at higher temperatures are expected to be smaller than those listed in table 4. Based on the observation that thermal activation of systems with high energy barriers for slip (and high PN stress) is less efficient than thermal activation of slip in systems with low barrier, we conjecture that increasing the temperature will preferentially reduce the critical stress of the low PN stress systems, and hence the overall ranking will not be significantly affected.

A further limitation of the present analysis is the constraint that dislocation lines remain straight under load. This is imposed by the periodic boundary conditions imposed in the y-direction in figure 5, and the associated small model size in the respective direction, which preclude kink nucleation.

In addition, non-Schmid effects representing the influence of the normal stress acting in the direction perpendicular to the glide plane on the PN stress, are likely to be significant in these crystals. These issues are subjects for further study.

5. Conclusion

Motivated by the potential role of slip and plasticity in reaction initiation, slip systems in β-HMX are identified and characterized using geometric analysis and molecular simulations. The geometric gamma surface, based on the volumetric overlap parameter, offers an intuitive and cost-effective way to rank slip systems. For the experimentally observed slip planes, (001) and (101), the overlap surfaces give good indication of which slip directions are likely.

Table 5. Components of macroscopic strain resulting from unit slip in specific slip systems.

Slip system	Plane normal	Burgers vector	ε_{11}	ε_{22}	ε_{33}	ε_{23}	ε_{13}	ε_{12}
(001)[100]	(0 0 1)	[1, 0, 0]	0.0	0.0	0.0	0.0	0.5	0.0
(101)[10$\bar{1}$]	(0.7, 0, 0.714)	[0.714, 0, −0.7]	0.5	0.0	−0.5	0.0	0.01	0.0
(101)[010]	(0.7, 0, 0.714)	[0, 1, 0]	0.0	0.0	0.0	0.357	0.0	0.35
(021)[100]	(0, 0.826, 0.564)	[1, 0, 0]	0.0	0.0	0.0	0.0	0.282	0.413
(011)[01$\bar{1}$]	(0, 0.591, 0.807)	[0.088, 0.803, −0.589]	0.0	0.475	−0.475	0.15	0.035	0.026
(011)[100]	(0, 0.591, 0.807)	[1, 0, 0]	0.0	0.0	0.0	0.0	0.403	0.295
(01$\bar{1}$)[011]	(0, 0.591, −0.807)	[−0.088, 0.803, 0.589]	0.0	0.475	−0.475	−0.15	0.035	−0.026
(01$\bar{1}$)[100]	(0, 0.591, −0.807)	[1, 0, 0]	0.0	0.0	0.0	0.0	−0.403	0.295

The PN stresses for the various slip systems shortlisted by the overlap procedure are computed using atomistic simulations. The results indicate that all dislocation cores are compact except for the (011)[01$\bar{1}$] system which exhibits core splitting for both edge and screw cases. The slip planes suitable for dislocation glide are (001), (101), (021) and {011}. The independent slip analysis indicates that these systems are sufficient for accommodating a general state of plastic strain, but that the twinning system must be always included in the list.

This study provides information that may be useful for developing mesoscale simulations aimed at illuminating the role of crystalline slip in hotspot initiation. In dislocation dynamics simulations, the PN stress is used as an activation stress for dislocation glide on various slip systems. Although the PN stress at ambient conditions is unknown, an Arrhenius type expression for activation energy (estimated from the PN stress) can be used as a first approximation. This analysis provides a ranking of slip systems which is likely to persist at finite temperatures. Furthermore, the geometric gamma surfaces can be used for other molecular crystals, as an efficient instrument towards inferring available slip systems.

Acknowledgment

This work was supported by US Air Force Research Labs (AFRL/RWK) through grant FA8651-16-1-0004.

ORCID iDs

Catalin R Picu https://orcid.org/0000-0001-8371-3564

References

[1] Bowden F P and Yoffe A 1948 Hot spots and the initiation of explosion *Symp. on Combustion, Flame and Explosion Phenomena* vol 3, pp 551–60
[2] Bowden F P and Yoffe A 1985 *Initiation and Growth of Explosion in Liquids and Solids* (Cambridge: Cambridge University Press)
[3] Bowden F P, Stone M A and Tudor G K 1947 Hot spots on rubbing surfaces and the detonation of explosives by friction *Proc. R. Soc.* A **188** 329–49
[4] Dick J J 1984 Effect of crystal orientation on shock initiation sensitivity of pentaerythritol tetranitrate explosive *Appl. Phys. Lett.* **44** 859–61
[5] Dick J J, Mulford R N, Spencer W J, Pettit D R, Garcia E and Shaw D C 1991 Shock response of pentaerythritol tetranitrate single crystals *J. Appl. Phys.* **70** 3572–87
[6] Dick J J and Ritchie J P 1994 The crystal orientation dependence of the elastic precursor shock strength in the PETN molecular explosive and the modeling of the steric hindrance to shear by molecular mechanics *J. Physique* IV **4** C8-393–98
[7] Millett J C F, Taylor P, Roberts A and Appleby-Thomas G 2017 The strength of two HMX based plastic bonded explosives during one dimensional shock loading *J. Dyn. Behav. Mater.* **3** 100–9
[8] Menikoff R and Sewell T D 2002 Constituent properties of HMX needed for mesoscale simulations *Combust. Theory Modelling* **6** 103–25
[9] Sorescu D C, Rice B M and Thompson D L 1998 Isothermal-isobaric molecular dynamics simulations of 1, 3, 5, 7-tetranitro-1, 3, 5, 7-tetraazacyclooctane (HMX) crystals *J. Phys. Chem.* B **102** 6692–5
[10] Cady H H and Smith L C 1962 *Studies on the Polymorphs of HMX* (Los Alamos, NM: Los Alamos Scientific Laboratory of the University of California)
[11] Myint P C and Nichols A L 2017 Thermodynamics of HMX polymorphs and HMX/RDX mixtures *Ind. Eng. Chem. Res.* **56** 387–403
[12] Korsunskii B L, Aldoshin S M, Vozchikova S A, Golovina N I, Chukanov N V and Shilov G V 2010 A new crystalline HMX polymorph: ε-HMX *Russ. J. Phys. Chem.* B **4** 934–41

[13] van der Heijden A E D M and Bouma R H B 2004 Crystallization and characterization of RDX, HMX, and CL-20 *Cryst. Growth Des.* **4** 999–1007
[14] Palmer S J P and Field J E 1982 The deformation and fracture of β-HMX *Proc. R. Soc.* A **383** 399–407
[15] Cady H H 1992 Growth and defects of explosives crystals *MRS Proc.* **296** 243–54 PROC-296-243
[16] Armstrong W R, Ammon H L, Du Z Y, Elban W L and Zhang X J 1992 Energetic crystal-lattice-dependent responses *MRS Proc.* **296** 227–32
[17] Gallagher H G, Miller J C, Sheen D B, Sherwood J N and Vrcelj R M 2015 Mechanical properties of β-HMX *Chem. Cent. J.* **9** 22
[18] Dick J J, Hooks D E, Menikoff R and Martinez A R 2004 Elastic–plastic wave profiles in cyclotetramethylene tetranitramine crystals *J. Appl. Phys.* **96** 374–9
[19] Barton N R, Winter N W and Reaugh J E 2009 Defect evolution and pore collapse in crystalline energetic materials *Modelling Simul. Mater. Sci. Eng.* **17** 035003
[20] Choi C S and Boutin H P 1970 A study of the crystal structure of β-cyclotetramethylene tetranitramine by neutron diffraction *Acta Crystallogr.* B **26** 1235–40
[21] Eiland P F and Pepinsky R 1954 The crystal structure of cyclotetramethylene tetranitramine *Z. Kristallogr.—Cryst. Mater.* **106** 273–98
[22] Kohno Y, Maekawa K, Azuma N, Tuchioka T, Hashizume T and Imamura A 1992 *Ab initio* calculations for a relationship between impact sensitivity and molecular structure in HMX polymorphs *Explosion Explosives* **53** 227–37
[23] Smith G D and Bharadwaj R K 1999 Quantum chemistry based force field for simulations of HMX *J. Phys. Chem.* B **103** 3570–5
[24] Hull D and Bacon D J 2001 *Introduction to Dislocations* (London: Butterworth-Heinemann)
[25] Munday L B, Solares S D and Chung P W 2012 Generalized stacking fault energy surfaces in the molecular crystal αRDX *Phil. Mag.* **92** 3036–50
[26] Hu X, Chen N and Li W 2016 A method for fast safety screening of explosives in terms of crystal packing and molecular stability *J. Mol. Model* **22** 170
[27] Nabarro F R N 1997 Fifty-year study of the Peierls–Nabarro stress *Mater. Sci. Eng.* A **234** (Suppl. C) 67–76
[28] Cai W, Bulatob V V, Chang J, Li J and Yip S 2003 Periodic image effects in dislocation modelling *Phil. Mag.* **83** 539–67
[29] Mathew N, Picu C R and Chung P W 2013 Peierls stress of dislocations in molecular crystal cyclotrimethylene trinitramine *J. Phys. Chem.* A **117** 5326–34
[30] Shinoda W, Shiga M and Mikami M 2004 Rapid estimation of elastic constants by molecular dynamics simulation under constant stress *Phys. Rev.* B **69** 134103
[31] Bedrov D, Ayyagari C, Smith G D, Sewell T D, Menikoff R and Zaug J M 2001 Molecular dynamics simulations of HMX crystal polymorphs using a flexible molecule force field *J. Comput. Aided Mater. Des.* **8** 77–85
[32] Sewell T D, Menikoff R, Bedrov D and Smith G D 2003 A molecular dynamics simulation study of elastic properties of HMX *J. Chem. Phys.* **119** 7417–26
[33] Lu L-Y *et al* 2009 The pressure-induced phase transition of the solid β-HMX *Mol. Phys.* **107** 2373–85
[34] Long Y, Liu Y G, Nie F D and Chen J 2012 A method to calculate the thermal conductivity of HMX under high pressure *Phil. Mag.* **92** 1023–45
[35] Zheng L and Thompson D L 2006 Molecular dynamics simulations of melting of perfect crystalline hexahydro-1,3,5-trinitro-1,3,5-s-triazine *J. Chem. Phys.* **125** 84505
[36] Akkbarzade H, Parsafar G A and Bayat Y 2012 Structural stability of nano-sized crystals of HMX: a molecular dynamics simulation study *Appl. Surf. Sci.* **258** 2226–30
[37] Rycroft C H 2009 VORO++: a three-dimensional Voronoi cell library in C++ *Chaos* **19** 41111
[38] Kroonblawd M P, Mathew N, Jiang S and Sewell T D 2016 A generalized crystal-cutting method for modeling arbitrarily oriented crystals in 3D periodic simulation cells with applications to crystal–crystal interfaces *Comput. Phys. Commun.* **207** (Suppl. C) 232–42
[39] Jacobson A, Panozzo D *et al* 2017 libigl: prototyping geometry processing research in C++ *SIGGRAPH Asia 2017 Courses (SA '17)* (New York: ACM) (https://doi.org/10.1145/3134472.3134497)
[40] Ayachit U 2015 *The ParaView Guide: A Parallel Visualization Application* (Clifton Park, NY: Kitware, Inc.)
[41] Plimpton S 1995 Fast parallel algorithms for short-range molecular dynamics *J. Comput. Phys.* **117** 1–19

[42] Barnett D M and Swasger L A 1971 The elastic energy of a straight dislocation in an infinite anisotropic elastic medium *Phys. Status Solidi* b **48** 419–28
[43] Hirth J P and Lothe J 1992 *Theory of Dislocations* (Malabar, FL: Krieger Publishing Company)
[44] Mathew N and Picu R C 2013 Slip asymmetry in the molecular crystal cyclotrimethylenetrinitramine *Chem. Phys. Lett.* **582** 78–81
[45] Mises R V 1928 Mechanik der plastischen Formänderung von Kristallen *Z. Angew. Math. Mech.* **8** 161–85
[46] Groves G W and Kelly A 1963 Independent slip systems in crystals *Phil. Mag.* A **8** 877–87
[47] Yoo M H 1981 Slip, twinning, and fracture in hexagonal close-packed metals *Metall. Trans.* A **12** 409–18